



Boosted Electrocatalytic Glucose Oxidation Reaction on Noble-Metal-Free MoO₃-Decorated Carbon Nanotubes

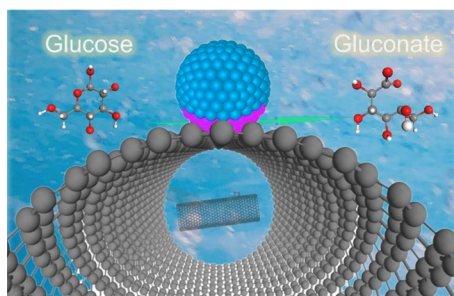
Yu-Long Men¹ · Ning Dou² · Yiyi Zhao¹ · Yan Huang¹ · Lei Zhang³ · Peng Liu¹

Received: 23 October 2023 / Revised: 25 November 2023 / Accepted: 1 December 2023 / Published online: 6 February 2024
© The Author(s) 2024

Abstract

Electrocatalytic glucose oxidation reaction (GOR) has attracted much attention owing to its crucial role in biofuel cell fabrication. Herein, we load MoO₃ nanoparticles on carbon nanotubes (CNTs) and use a discharge process to prepare a noble-metal-free MC-60 catalyst containing MoO₃, Mo₂C, and a Mo₂C–MoO₃ interface. In the GOR, MC-60 shows activity as high as 745 μA/(mmol/L cm²), considerably higher than those of the Pt/CNT (270 μA/(mmol/L cm²)) and Au/CNT catalysts (110 μA/(mmol/L cm²)). In the GOR, the response minimum on MC-60 is as low as 8 μmol/L, with a steady-state response time of only 3 s. Moreover, MC-60 has superior stability and anti-interference ability to impurities in the GOR. The better performance of MC-60 in the GOR is attributed to the abundant Mo sites bonding to C and O atoms at the MoO₃–Mo₂C interface. These Mo sites create active sites for promoting glucose adsorption and oxidation, enhancing MC-60 performance in the GOR. Thus, these results help to fabricate more efficient noble-metal-free catalysts for the fabrication of glucose-based biofuel cells.

Graphical abstract



Keywords Interface effect · Electrocatalysis · Molybdenum oxide · Glucose · Oxidation reaction

Introduction

Glucose (C₆H₁₂O₆) is one of the most common biomasses. Among various reactions related to glucose, the electrocatalytic glucose oxidation reaction (GOR) has attracted great attention [1]. The GOR plays a crucial role in constructing glucose-based biofuel cells for solving energy and environmental concerns [1, 2]. The GOR is also a key reaction in the fabrication of sophisticated devices

that detect trace glucose in blood and food [2–5]. Noble metal catalysts, e.g., Au- and Pt-based catalysts, are the most widely used catalysts for the GOR because of their high catalytic activity, which is usually evaluated by the electronic current (μA) originating from detecting and converting 1 mmol/L (mM) glucose on a 1 cm² electrode coated by catalysts. For example, the PdCuPt nanocrystal catalyst with multibranches exhibited an activity of 378 μA/(mmol/cm²) in the GOR. However, noble metal catalysts still suffer from poor response to trace glucose and low anti-interference ability to impurities [2]. Additionally, high prices and scarce resources of noble metals

Yu-Long Men and Ning Dou have contributed equally to this work.

Extended author information available on the last page of the article

limit the large-scale commercialization of noble metal catalysts. Efficient noble-metal-free catalysts for the GOR are thereby highly desired.

Many noble-metal-free catalysts have been developed for the GOR, e.g., transition metal oxides, transition metal phosphates, transition metal sulfides, and carbon nanofibers [6–12]. Wang et al. [7] fabricated a NiCo–NiCoO₂/carbon hollow cage catalyst for the GOR and obtained an improved GOR activity of 340.4 $\mu\text{A}/(\text{mmol/L cm}^2)$ and good long-term stability. This good performance was attributed to the high electronic conductivity, large surface area, and fast ion/electron transfer at the electrode and electrolyte–electrode interface on the NiCo–NiCoO₂/carbon hollow cage catalyst [7]. Mao et al. [8] filled NiS/Ni(OH)₂ nanosheets in hollow interiors of ammonium polyacrylate-functionalized polypyrrole nanotubes (NH₄PA/PPyNTs) to form NiS/Ni(OH)₂/NH₄PA/PPyNTs catalyst. In the GOR, NiS/Ni(OH)₂@NH₄PA/PPyNTs exhibited improved performance, with a detection limit of only 3.1 $\mu\text{mol/L}$ (the lowest glucose concentration that the catalyst can respond to) [8]. Furthermore, ionizable NH₄PA and good conductive PPyNTs promoted electronic transmission as well as the transport of glucose and products, whereas NiS/Ni(OH)₂ nanosheets provided more abundant catalytic active sites [8]. This characteristic was shown to be the origin of the improved GOR performance of NiS/Ni(OH)₂@NH₄PA/PPyNTs [8]. Peng et al. [11] reported that the activity of the carbon-layer-coated tungsten oxide nanosphere catalyst in the GOR was higher than that of the pure tungsten oxide nanosphere catalyst without carbon. Coating a carbon layer with a thickness of 15 nm on a tungsten oxide nanosphere created oxygen vacancies on the surface of tungsten oxide nanospheres, and these vacancies enhanced electron transfer between the catalyst and reactants (H₂O and glucose), promoting glucose oxidation by O or/and OH groups formed from H₂O dissociation [11]. This result was proposed to be the origin of the higher activity of the carbon-layer-coated tungsten oxide nanosphere catalyst in the GOR [11]. Despite extensive studies, the performance of the noble-metal-free catalyst in the GOR, including activity, response time, stability, and anti-interference ability to impurities, are still below the requirements of commercialization and need further improvements.

Herein, we coat MoO₃ nanoparticles on carbon nanotubes (CNTs) to form a noble-metal-free MC-60 catalyst by a discharge process under an argon (Ar) atmosphere (Figs. 1a, S1, and S2). In the GOR, MC-60 exhibits an activity of 745 $\mu\text{A}/(\text{mmol/L cm}^2)$. This activity is higher than those on a CNT-supported Pt catalyst (Pt/CNT) (270 $\mu\text{A}/(\text{mmol/L cm}^2)$) and a CNT-supported Au catalyst (Au/CNT) (110 $\mu\text{A}/(\text{mmol/L cm}^2)$). Moreover, MC-60 has superior stability and anti-interference ability to impurities in the GOR. The improved performance of MC-60 in the GOR is due to the abundant Mo sites bonding to C and O atoms at the

MoO₃–Mo₂C interface, which serve as active sites for glucose adsorption and oxidation.

Experimental Section

Catalyst Preparation

Figure 1a illustrates the preparation process of catalysts. Ammonium molybdate (AMT, 170 mg) was first loaded on CNT (200 mg) via wet impregnation. Second, the sample obtained in the first step was dried at 60 °C for 12 h, forming the CNT-supported AMT (AMT/CNT). Third, AMT/CNT was treated by the discharge process for 20 min, affording a catalyst MC-20. Elongating the discharge process conducted on AMT/CNT to 60 min produced the MC-60 catalyst. For comparison, we also prepared a Mo₂C/CNT catalyst using the following steps. First, AMT (170 mg) and glucose (510 mg) were loaded on CNTs (200 mg) via wet impregnation. Second, the impregnated sample was dried at 60 °C for 12 h. Third, the dried sample was treated by the discharge process for 60 min, forming the Mo₂C/CNT catalyst.

The set-up of the discharge process is shown in Figs. S1 and S2. In the discharge process, a 500 mg sample was first placed in the discharge chamber. Subsequently, Ar was introduced into the discharge chamber. Next, 100 V was applied to the electrodes of the discharge chamber to trigger the discharge process. The discharge process proceeds at atmospheric pressure without heating. The temperature of the discharge process is below 150 °C, lower than the temperature traditionally used for dissociating AMT (> 200 °C) [13–16]. During the discharge process, abundant electrons with energies of 5–10 eV are produced from Ar ionization and move at high speeds in the discharge chamber. Collisions of the electrons with other species can efficiently dissociate metal salts into metal oxides, reduce metal ions into metal atoms, control the transfer and aggregation of metal atoms to form metal nanoparticles with uniform sizes, and trigger various reactions among different species [13–16]. Further details regarding the discharge process have been reported in our previous work [16–18].

Catalyst Characterization

A PANalytical X'Pert powder X-ray diffraction meter with Cu K α radiation was applied to observe the X-ray diffraction (XRD) patterns of catalysts. Raman spectra were obtained on equipment (Jobin–Yvon LabRam HR800) with an Ar laser (514 nm). X-ray photoelectron spectroscopy (XPS) observations were conducted on an AXIS UltraDLD spectrometer. All binding energies were calibrated using the C 1s peak at 284.8 eV. Specific surface areas of catalysts were measured on a micromeritics ASAP 2020 adsorption analyzer

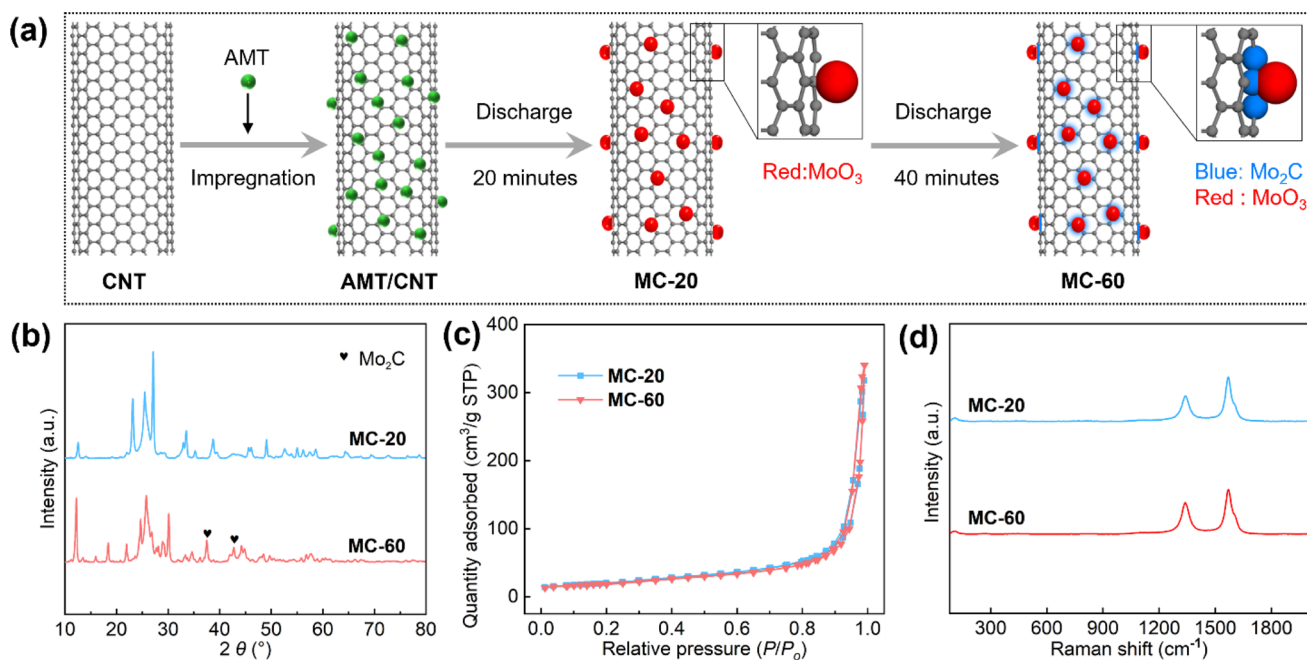


Fig. 1 Catalyst preparation and characterization. **a** Schematic for preparing catalysts; **b** XRD patterns; **c** N₂ adsorption–desorption curves; **d** Raman spectra

and calculated using the Brunauer–Emmett–Teller (BET) method. Transmission electron microscopy (TEM) observations, including high-resolution TEM (HRTEM), high-angle annular dark field, and elemental mapping images, were performed on a transmission electron microscope (FEI Titan G2 80-200 Chemi STEM).

Electrochemical Measurements

A workstation (CHI760E, CH Instrument, Inc.) with a three-electrode system comprising a working electrode, counter electrode, and reference electrode was used to perform electrochemical measurements at room temperature. Loading the catalyst on a circular glassy carbon electrode with a diameter of 0.3 cm produced the working electrode. A Pt plate electrode (0.5 mm × 0.5 mm) and a saturated calomel electrode (SCE) were the counter and reference electrodes, respectively. To activate these electrodes and stabilize the reaction system, 20 cycles of cyclic voltammetry (CV) scans were performed at 100 mV/s from −1 to 1 V (vs. SCE) before the experiments. The electrocatalytic oxygen evolution reaction (OER) from H₂O was performed in a 100 mL aqueous solution containing 0.1 mol NaOH. The potential was calculated using Eq. (1):

$$E_{\text{RHE}} = E_{\text{SCE}} + 0.2415 + 0.0591 \times \text{pH} \quad (1)$$

E_{SCE} and E_{RHE} were obtained against the SCE and calibrated versus the reversible hydrogen electrode (RHE),

respectively. Linear sweep voltammetry (LSV) polarization curves were recorded at 5 mV/s with a 90% iR (internal resistance) compensation. The overpotential at 10 mA/cm² (η_{10}) was calculated by subtracting 1.23 V from the potential (E_{RHE}) at 10 mA/cm² on the LSV curve. To calculate electrochemical double-layer capacitance (C_{DL}), Δj was first obtained from Eq. (2):

$$\Delta j = j_{\text{oxidation}} - j_{\text{reduction}} \quad (2)$$

Here, $j_{\text{oxidation}}$ and $j_{\text{reduction}}$ are current densities on the oxidation and reduction parts of the CV curves, respectively; Δj was then plotted as a function of the scan rate and linear fitting of the Δj –(scan rate) curve obtained C_{DL} . Linear fitting on the Tafel curve deduced from the LSV curve led to the Tafel slope.

The reaction solution for the GOR was similar to that for OER (aqueous solution with 0.1 mol/L NaOH, 100 mL), except that a certain amount of glucose was added to the solution. The relationship between current density and glucose concentration was deduced according to CV scans obtained at different glucose concentrations. Before the GOR, the reaction solution was stirred at a speed of 200 r/min for 2 min to ensure fast and uniform dispersion of glucose. All tests were performed in a static solution without stirring. The current density as a function of time and the immediate response were obtained at a 500 mV potential (vs. SCE).

Results and Discussion

Catalyst Characterization

As depicted in Fig. 1b, MC-20 exhibits XRD peaks at 12.6°, 14.1°, 21.9°, 23.2°, 25.5°, 27.3°, 28.6°, 29.4°, 32.9°, 33.6°, 35.2°, 38.7°, 39.4°, 45.6°, 46.0°, 49.2°, 52.7°, 53.9°, 54.9°, 56.2°, 57.4°, 58.7°, 64.3°, 69.5°, 72.8°, 76.3°, and 78.6°, with the peak appear at 25.5° being attributed CNTs (PDF#75-1621) and other peaks being attributed MoO₃ (PDF#76-1003). In the XRD pattern of MC-60 (Fig. 1b), in addition to the peaks of CNTs and MoO₃, peaks at 18.4°, 34.6°, 38.1°, 42.4°, 44.7°, 48.6°, 49.7°, and 67.3° are attributed to Mo₂C (PDF#75-1621). This result indicates that MC-20 is composed of CNTs and MoO₃, while MC-60 contains CNTs, MoO₃, and Mo₂C. Abundant electrons are produced in the discharge process during catalyst preparation [13–18]. When conducting the discharge process to treat AMT/CNTs for 20 min, collisions of the electrons produced during the discharge process with AMT result in the dissociation of AMT to MoO₃, producing MC-20 containing CNTs and MoO₃ [13–18]. When the discharge process is increased

to 60 min, in addition to the dissociation of AMT from MoO₃, collisions of the electrons produced during the discharge process with Mo species and CNTs create Mo–C bonds, thus affording MC-60 that contains CNTs, MoO₃, and Mo₂C [13–18]. N₂ adsorption–desorption experiments (Fig. 1c) reveal that surface areas of MC-20 (70.95 m²/g) and MC-60 (70.55 m²/g) are similar. The Raman spectra of MC-20 and MC-60 (Fig. 1d) are almost identical and show peaks at 1332 and 1581 cm⁻¹, respectively, due to CNTs [16–18].

As per the TEM images (Figs. 2 and S3), MoO₃ nanoparticles are dispersed on CNTs on MC-20 and MC-60. Lattice fringes with a distance of 0.340 nm observed on MC-20 and MC-60 are due to the (002) plane of CNTs (Fig. 2a and b) [16]. MoO₃ nanoparticles on MC-20 have an average size of (12.1 ± 0.8 nm) (Fig. S3). In addition to their presence on CNTs, lattice fringes with a distance of 0.233 nm are also found on MC-20 and attributed to the (131) plane of MoO₃ (Fig. 2a). The average size of the MoO₃ nanoparticles on MC-60 (11.6 ± 0.7 nm) (Fig. S3) is close to that on MC-20. In addition to appearing on CNTs, lattice fringes with distances of 0.233, 0.212, and 0.201 nm are also observed on MC-60 and are caused by MoO₃(131) (PDF#76-1003),

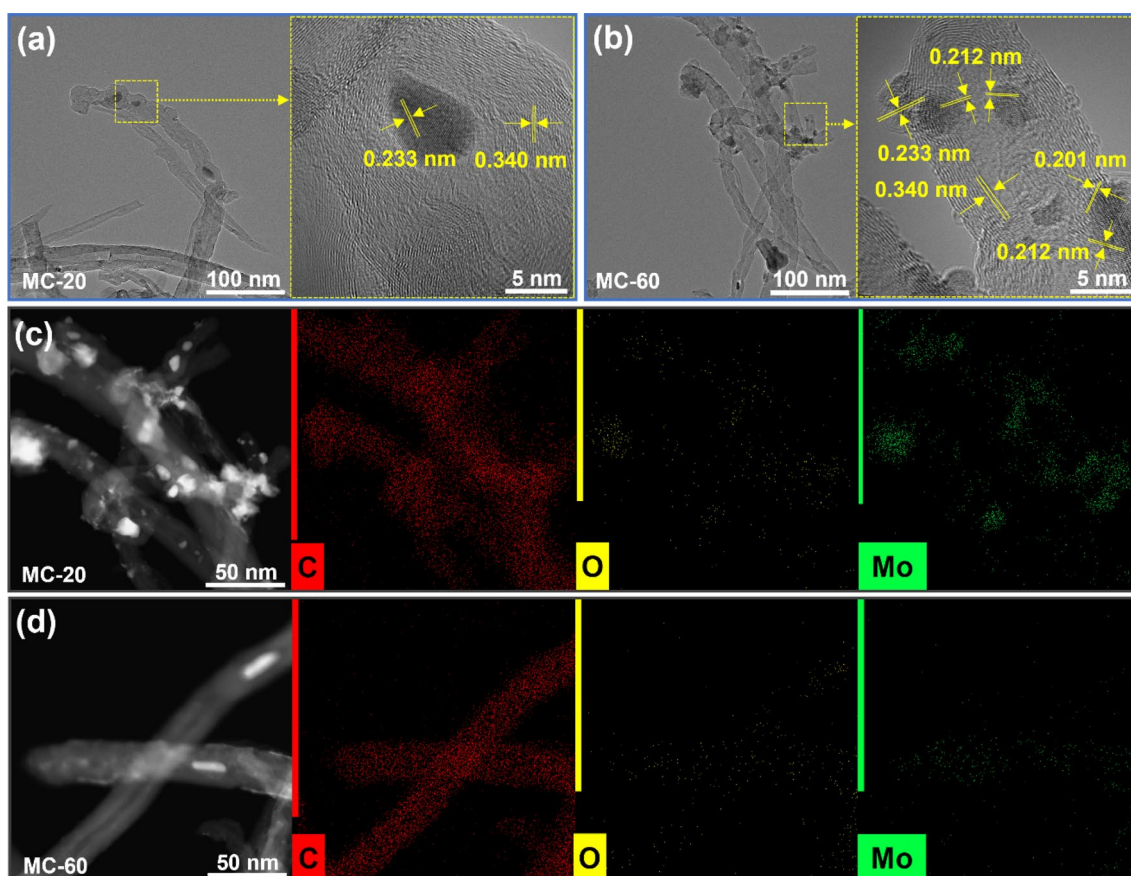


Fig. 2 Catalyst morphologies. **a** TEM and HRTEM images of MC-20; **b** TEM and HRTEM images of MC-60; **c** Elemental mapping images of MC-20; **d** Elemental mapping images of MC-60

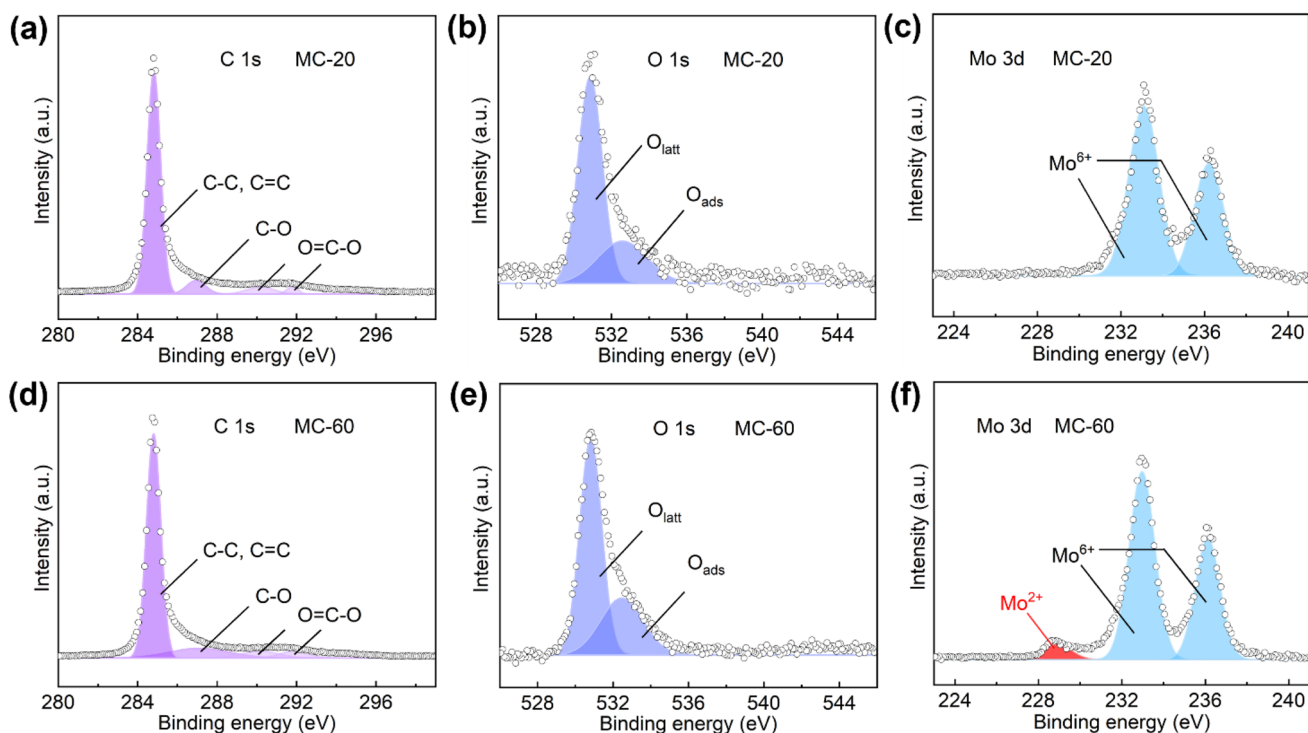


Fig. 3 Surface properties of catalysts. **a** C 1s, **b** O 1s and **c** Mo 3d XPS spectra for MC-20. **d** C 1s, **e** O 1s and **f** Mo 3d XPS spectra for MC-60

Mo₂C(112) (PDF#75-1621), and Mo₉O₂₆(020) (PDF#05-0441) planes, respectively (Fig. 2b). This result reveals Mo₂C formation on MC-60. When treating metal oxides with the discharge process, collisions of discharge process electrons with metal oxides create oxygen vacancies on metal oxides [13–16]. Thus, oxygen vacancies are formed on MoO₃ of MC-60 during the discharge process. This outcome could be the origin of Mo₉O₂₆ on MC-60. Elemental mapping patterns confirm the presence of C, Mo, and O on MC-20 and MC-60 (Fig. 2c and d).

Full-range survey XPS spectra confirm the presence of C, O, and Mo on MC-20 and MC-60 (Fig. S4). Thus, the C 1s XPS spectrum of MC-20 exhibits four peaks at 284.8, 286.9, 290.2, and 291.8 eV (Fig. 3a). The peak at 284.8 eV is due to C–C and C=C bonds in CNTs, and the peak at 286.9 eV is caused by the C–O bond formed between C atoms and OH groups on CNTs [17–23]. Peaks at 290.2 and 291.8 eV are due to O=C–O bonds in COOH groups on CNTs [17–23]. The O 1s XPS spectrum of MC-20 has two peaks at 531.1 and 532.4 eV, characteristic of O atoms in the lattice of MoO₃ (O_{latt}) and OH or/and COOH groups on CNTs (O_{ads}) [17–25]. The Mo 3d XPS spectrum of MC-20 can be fitted into two peaks at 233.2 and 236.3 eV (Fig. 3c), which are due to Mo⁶⁺ in MoO₃ [22, 23]. The C 1s XPS spectrum of MC-60 (Fig. 3d) is similar to that of MC-20, indicating that a longer discharge process for catalyst preparation did not influence CNT features. Compared with those of MC-20, the

O 1s XPS peaks of MC-60 (Fig. 3e) shift to lower binding energies. This shift could be due to the electronic interactions between MoO₃ nanoparticles and CNTs. Mo 3d XPS peaks due to Mo⁶⁺ in MoO₃ on MC-60 are located at 232.9 and 236.1 eV, lower than those on MC-20. This comparison further implies electronic interactions between MoO₃ nanoparticles and CNTs on MC-60. In the Mo 3d XPS spectrum of MC-60, in addition to the peaks of Mo⁶⁺ in MoO₃, a peak appears at 228.1 eV and is assigned to Mo²⁺ in Mo₂C (Fig. 3f) [22–25]. These XPS spectra demonstrate that Mo₂C is negligible on MC-20 but present on MC-60.

MC-20 is prepared by conducting a 20 min discharge process on AMT/CNT (Fig. 1a). As depicted by XPS spectra (Fig. 3a–c), the Mo-containing species on MC-20 is MoO₃, and no other Mo-containing species such as AMT and Mo₂C are on MC-20. Thus, the 20 min discharge process can completely dissociate AMT into MoO₃ but cannot produce Mo₂C. Increasing the discharge process time from 20 to 60 min leads to Mo₂C formation, as reflected by XPS spectra (Fig. 3d–f). Mo₂C could be produced from the reaction of Mo atoms of MoO₃ with C atoms of CNTs, rather than the reaction of AMT with CNTs, as AMT was completely dissociated into MoO₃ in the 20-min discharge process. To explore how the time of the discharge process affects Mo₂C formation, Mo 3d XPS spectra of catalysts prepared using 20, 40, 60, 90, and 120 min discharge processes are compared (Fig. S5). By increasing the discharge process time

from 20 to 120 min, the Mo 3d XPS peak of Mo^{2+} of Mo_2C becomes stronger. According to Mo 3d XPS spectra, the ratios of $\text{Mo}_2\text{C}/\text{MoO}_3$ on catalysts prepared using 20, 40, 60, 90, and 120 min discharge processes are calculated to be 0, 0.06, 0.11, 0.15, and 0.18, respectively. Thus, Mo_2C content on the catalyst increases when increasing the discharge process time for catalyst preparation from 20 to 120 min. Mo_2C is formed in two ways. First, during a discharge process longer than 20 min, collisions of discharge process electrons with MoO_3 nanoparticles and CNTs trigger the reaction of Mo atoms of MoO_3 nanoparticles and C atoms of CNTs at the MoO_3 -CNT interface, producing Mo_2C there. Second, during a discharge process longer than 20 min, collisions of discharge process electrons with CNTs induce a transfer of C atoms from CNTs to MoO_3 nanoparticles, triggering the reaction of Mo atoms with C atoms. This produces Mo_2C on MoO_3 nanoparticles. Mo_2C formations on MC-60, at the MoO_3 -CNT interface or on MoO_3 nanoparticles, create the Mo_2C - MoO_3 interface on MC-60.

GOR Performance of Catalysts

During the GOR process, OER inevitably occurs [2–10, 17]. Moreover, O atoms and OH groups formed from OER are key species for glucose oxidation in the GOR. Thus, before exploring the performance of catalysts in the GOR, their performance in OER is first studied. Figure 4a illustrates CV curves for CNTs, MC-20, and MC-60 in OER. Pure CNT has no activity to OER. MC-20 and MC-60 are active to OER, with the activity of MC-60 higher than that of MC-20. According to LSV polarization curves (Fig. 4b), η_{10} for MC-20 and MC-60 is calculated to be 450 and 410 mV, respectively. Thus, to produce a $10 \text{ mA}/\text{cm}^2$ current, 410 mV and 450 mV potentials are needed on MC-60 and MC-20, respectively. This result confirms that MC-60 has a higher activity to OER than MC-20. The electrochemical active surface area (ECSA) is evaluated by measuring C_{DL} in a potential range without a Faradic process at scan rates of 20, 40, 60, 80, 100, and 120 mV/s (Fig. S6). As shown in Fig. 4c, the C_{DL} of CNT, MC-20, and MC-60 are 2.0, 8.8, and $10.0 \mu\text{F}/\text{cm}^2$, respectively. Thus, the ECSA of CNT, MC-20, and MC-60 are 0.05, 0.22, and 0.25, respectively.

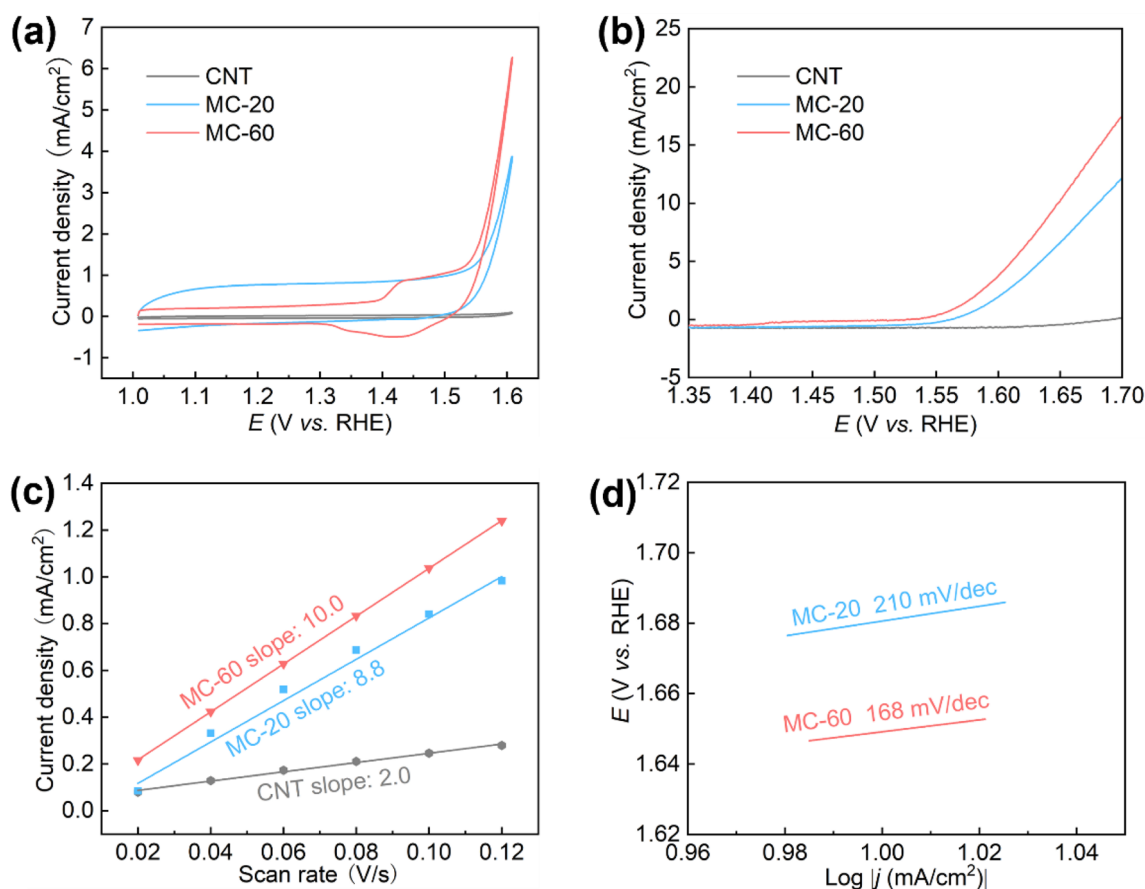


Fig. 4 OER performance of catalysts. **a** CV curves; **b** LSV polarization curves measured at a scan rate of 5 mV/s; **c** Current density as a function of scan rate in a non-faradic range; **d** Tafel curves and slopes

The larger ECSA could be responsible for the higher OER activity of MC-60. The Tafel slopes of MC-20 and MC-60 are measured to be 210 and 168 mV/dec, respectively (Fig. 4d). The smaller Tafel slope reveals that the reaction rate is faster on MC-60 than on MC-20. These results show that MC-60 has higher activity and faster kinetics in OER than MC-20.

The reaction system for the GOR has a certain amount of added glucose, but otherwise is similar to that for OER. We first explore the performances of MC-20 and MC-60 in the GOR in an aqueous solution (0.1 mol NaOH) containing 5 mmol/L glucose, as depicted in Fig. 5a. Compared with those obtained in the absence of glucose (Fig. 4a), the CV curves of MC-20 and MC-60 with 5 mmol glucose added to the reaction solution exhibit evident peaks from 1.35 to 1.55 V, which are caused by the reduction and oxidation of glucose [5–11]. This comparison reveals that the GOR is triggered by MC-20 and MC-60. Compared with those of MC-20, the reduction and oxidation peaks of glucose in the CV curves of MC-60 are stronger. Thus, MC-60 has higher activity in the GOR than MC-20. We next explore the CV curves of MC-20 and MC-60 at different glucose concentrations (C_{glucose}) (Fig. S7). The current density (j) at the top of the glucose oxidation peak on the CV curve in Fig. S7 is plotted as a function of C_{glucose} in Fig. 5b. The j - C_{glucose} relationships are well fitted by straight lines for MC-20 (Eq. (3)) and MC-60 (Eq. (4)):

$$j = 0.026 \times C_{\text{glucose}} + 0.4 \quad (3)$$

$$j = 0.745 \times C_{\text{glucose}} + 5.7 \quad (4)$$

The slope of the j - C_{glucose} line corresponds to the activity of the catalyst in the GOR, i.e., the electronic current (μA) originating from detecting and converting 1 mmol glucose on a 1 cm² electrode coated by the catalyst. According to the j - C_{glucose} lines in Fig. 5b, the activity of MC-60 in the GOR is 745 $\mu\text{A}/(\text{mmol/L cm}^2)$, 28.6-fold higher than that of MC-20 (26 $\mu\text{A}/(\text{mmol/L cm}^2)$).

Catalysts prepared using different discharge process times exhibit different activities in the GOR. As illustrated in Fig. 5c, when increasing the discharge process time from 20 to 120 min, the GOR activity of the catalyst first increases from 26 to 745 $\mu\text{A}/(\text{mmol/L cm}^2)$ and then decreases to 232 $\mu\text{A}/(\text{mmol/L cm}^2)$, with the highest GOR activity being achieved on MC-60. We also examine the activity of the Mo₂C/CNT catalyst in the GOR. The Mo 3d XPS spectrum of Mo₂C/CNT (Fig. S8) shows Mo₂C peaks but not MoO₃ peaks, indicating that MoO₃ is negligible on Mo₂C/CNT. Moreover, the GOR activity of Mo₂C/CNT is $\mu\text{A}/(\text{mmol/L cm}^2)$, which is much lower than that of MC-60. Additionally, in our previous work, we explored

the performance of Pt/CNT and Au/CNT catalysts in the GOR [11, 17, 26]. The activity of MC-60 in the GOR is also higher than those of Pt/CNT (270 $\mu\text{A}/(\text{mmol/L cm}^2)$) and Au/CNT (110 $\mu\text{A}/(\text{mmol/L cm}^2)$). The detection limit (response minimum) reflects the sensitivity of the catalyst in the GOR and is measured by recording the amperometric response (Fig. 5d). A lower detection limit indicates that the catalyst has a higher sensitivity in the GOR. By successively adding a certain amount of glucose to the reaction solution, the current density on MC-60 shows step-like changes representing the response of MC-60 to the GOR. The step-like current density response is still evident at a C_{glucose} as low as 8 $\mu\text{mol/L}$ (μM) and disappears when C_{glucose} is lower than 8 $\mu\text{mol/L}$. Thus, the detection limit of MC-60 in the GOR is 8 μmol . The steady-state response time of MC-60 at a C_{glucose} of 8 $\mu\text{mol/L}$ is only 3 s. The detection limit on MC-20 is 200 μmol , 25-fold larger than that of MC-60 (Fig. S9). Moreover, the steady-state response time of MC-20 (10 s, Fig. S9) is much longer than that of MC-60. This comparison further demonstrates the higher efficiency of MC-60 in the GOR.

To measure the anti-interference ability of the catalyst to impurities during the GOR, we continuously add glucose (0.1 mmol), urea (0.1 mmol), glutamic acid (0.1 mmol), oxalic acid (0.1 mmol), citric acid (0.1 mmol), amyllum (0.1 mmol), chitosan (0.1 g/L), and NaCl (0.1 mmol) to the reaction solution. When glucose is added to the reaction solution, MC-60 shows a fast and strong response; when other species are added, there is no response (Fig. 5e), revealing the excellent anti-interference ability of MC-60 to impurities during the GOR. The current density remains almost unchanged after proceeding with the GOR for 30 h on MC-60, but it decreases by 20% after proceeding with the GOR for 10 h on MC-20. This comparison indicates that MC-60 has a higher stability in the GOR (Fig. 5f).

Discussion

As previously mentioned, MC-60 containing MoO₃ and Mo₂C considerably outperforms the MoO₃/CNT catalyst without Mo₂C (MC-20) in the GOR. Next, we discuss the origin of this difference in performance. The morphologies, MoO₃ nanoparticle sizes, and surface areas of MC-60 and MC-20 are similar and, therefore, not the origins of the difference. An evident difference between MC-60 and MC-20 is that Mo₂C is negligible on MC-20 but present on MC-60. The presence of Mo₂C on MC-60 at the MoO₃-CNT interface or on MoO₃ nanoparticles creates a Mo₂C-MoO₃ interface on MC-60. This interface could influence glucose adsorption and oxidation on MC-60.

To elucidate the influence of the Mo₂C-MoO₃ interface on glucose adsorption and oxidation, we explore

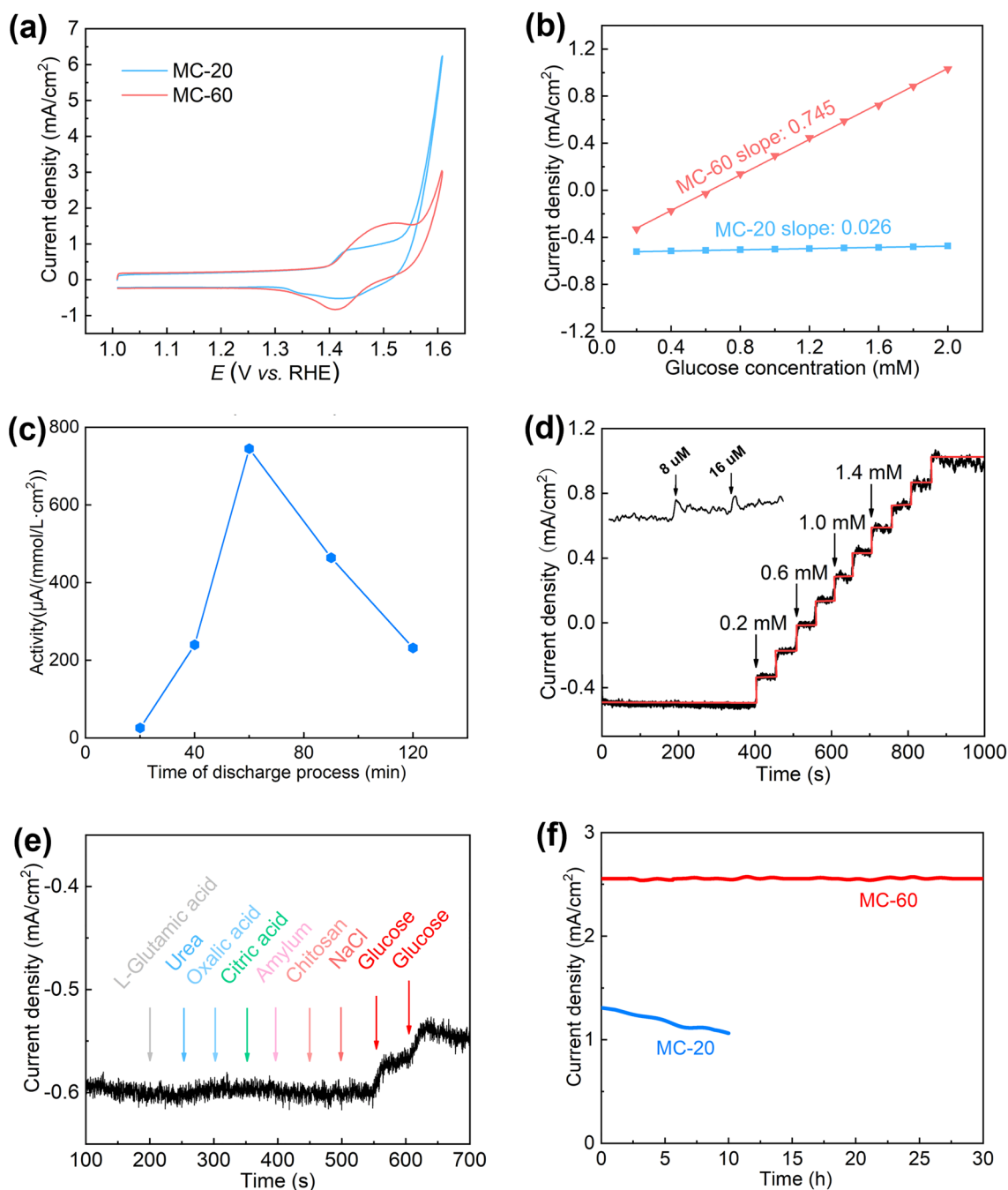


Fig. 5 GOR performance of catalysts. **a** CV curves; **b** Current density as a function of C_{glucose} ; **c** Activity of catalysts prepared using different discharge times; **d** Current density measured when adding different C_{glucose} into reaction solution at different times for MC-60; **e** Current density measured when continuously adding glucose

(0.1 mmol/L), urea (0.1 mmol/L), glutamic acid (0.1 mmol/L), oxalic acid (0.1 mmol/L), citric acid (0.1 mmol/L), amyllum (0.1 mmol/L), chitosan (0.1 g/L) and NaCl (0.1 mmol/L) into reaction solution at different times (0.5 V vs. SCE) for MC-60. **f** Stability of MC-20 and MC-60 in GOR

the glucose adsorption and oxidation on pure MoO_3 , the $\text{MoO}_3/\text{Mo}_2\text{C}$ composite with Mo–C bonds at the $\text{MoO}_3\text{--Mo}_2\text{C}$ interface, and pure Mo_2C using density functional theory (DFT) calculations. Details of the DFT calculation method and structures for modeling these systems are shown in supplementary information (Fig. S10).

The adsorption energy (E_a) of glucose on a catalyst is calculated using Eq. (5):

$$E_a = E_{(\text{glucose-catalyst})} - E_{\text{glucose}} - E_{\text{catalyst}} \quad (5)$$

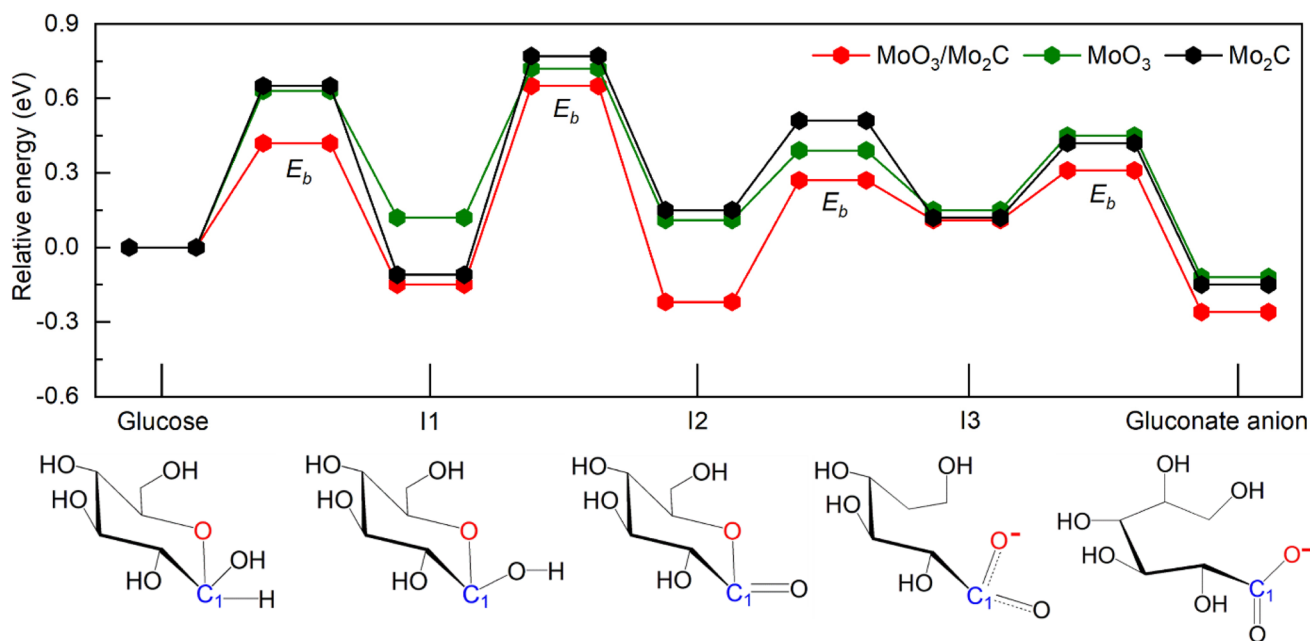


Fig. 6 E_r and E_b for glucose oxidation to gluconate anion on pure MoO₃, MoO₃/Mo₂C composite and pure Mo₂C as well as molecular structure of the species included in the oxidation process

Positive and negative E_a values represent endothermic and exothermic adsorption, respectively. Therefore, a more negative E_a indicates a more favorable adsorption of glucose on the catalyst. On pure MoO₃ and pure Mo₂C, the Mo site is most favorable for glucose adsorption, with E_a of -0.12 and -0.25 eV, respectively (Fig. S10). On the MoO₃/Mo₂C composite with Mo–C bonds at the MoO₃–Mo₂C interface, Mo site bonding to C and O atoms at this interface is most favorable for glucose adsorption, with an E_a of -0.68 eV (Fig. S10). This result indicates that the MoO₃/Mo₂C composite with Mo–C bonds at the MoO₃–Mo₂C interface promotes glucose adsorption, compared with pure MoO₃ and pure Mo₂C.

Previous studies have shown that during the GOR, the product of glucose oxidation by O or/and OH groups produced from H₂O dissociation is gluconate anion, and glucose oxidation to gluconate anion proceeds along with the formation of intermediates I1–I3 (Fig. 6) [17, 27–30]. Figure 6 shows the oxidation process as well as the DFT-calculated reaction energy (E_r) and energy barrier (E_b) of each step on pure MoO₃, the MoO₃/Mo₂C composite with Mo–C bonds at the MoO₃–Mo₂C interface, and pure Mo₂C. As shown by E_r and E_b in Fig. 6, glucose oxidation is more favorable on the MoO₃/Mo₂C composite with Mo–C bonds at the MoO₃–Mo₂C interface than on pure MoO₃ and pure Mo₂C, thermodynamically and kinetically. Thus, the MoO₃/Mo₂C composite with Mo–C bonds at the MoO₃–Mo₂C interface promotes glucose oxidation, compared with pure MoO₃ and pure Mo₂C.

Based on the DFT calculations, bonding of Mo with C and O at the MoO₃–Mo₂C interface promotes adsorption and oxidation. Mo₂C formation on MC-60 at the MoO₃–CNT interface or on MoO₃ nanoparticles creates abundant Mo sites, wherein Mo bonds to C and O atoms to promote glucose adsorption and oxidation. This occurrence could be the origin of the better performance of MC-60 in the GOR. However, excess Mo₂C on CNT-supported MoO₃ nanoparticle catalysts decreases the number of MoO₃, thus decreasing the amount of Mo sites bonding to C and O atoms. This occurrence could be the origin of the decreased GOR performance of catalysts that have more Mo₂C including catalysts prepared using the 90 and 120 min discharge processes as well as the Mo₂C/CNT catalyst (Fig. 5c). The ratio of Mo₂C/MoO₃ in MC-60 is 0.11. Therefore, on the CNT-supported MoO₃ catalysts, this ratio should be controlled near 0.11.

Conclusion

In summary, we loaded MoO₃ nanoparticles on CNTs and used a discharge process to form a noble-metal-free MC-60 catalyst containing a Mo₂C–MoO₃ interface. In the GOR, MC-60 shows activity as high as 745 $\mu\text{A}/(\text{mmol/L cm}^2)$, 28.6-fold higher than that on catalysts without a Mo₂C–MoO₃ interface (26 $\mu\text{A}/(\text{mmol/L cm}^2)$) and higher than those on the Pt/CNT catalyst (270 $\mu\text{A}/(\text{mmol/L cm}^2)$) and the Au/CNT catalyst (110 $\mu\text{A}/(\text{mmol/L cm}^2)$). In the GOR, the response minimum on MC-60 is as low as

8 $\mu\text{mol/L}$, with a steady-state response time of only 3 s. Moreover, MC-60 has superior stability and anti-interference ability to impurities in the GOR. The better performance of MC-60 in the GOR is due to abundant Mo sites bonding to C and O atoms at the $\text{MoO}_3\text{-Mo}_2\text{C}$ interface. The Mo sites bonding to C and O atoms at the $\text{MoO}_3\text{-Mo}_2\text{C}$ interface create active sites promoting glucose adsorption and oxidation, thus enhancing the performance of MC-60 in the GOR. These results help fabricate more efficient noble-metal-free catalysts for glucose-based biofuel cells.

Supplementary Information The online version contains supplementary material available at <https://doi.org/10.1007/s12209-023-00378-7>.

Acknowledgements This work is supported by the National Natural Science Foundation of China (Nos. 82170426 and 22078193) and Double Thousand Plan of Jiangxi Province (Nos. 461654, jxsq2019102052).

Declarations

Conflict of interest The authors declare that there is no conflict of interest.

Open Access This article is licensed under a Creative Commons Attribution 4.0 International License, which permits use, sharing, adaptation, distribution and reproduction in any medium or format, as long as you give appropriate credit to the original author(s) and the source, provide a link to the Creative Commons licence, and indicate if changes were made. The images or other third party material in this article are included in the article's Creative Commons licence, unless indicated otherwise in a credit line to the material. If material is not included in the article's Creative Commons licence and your intended use is not permitted by statutory regulation or exceeds the permitted use, you will need to obtain permission directly from the copyright holder. To view a copy of this licence, visit <http://creativecommons.org/licenses/by/4.0/>.

References

1. Bag S, Baksi A, Nandam SH et al (2020) Nonenzymatic glucose sensing using $\text{Ni}_{60}\text{Nb}_{40}$ nanoglass. *ACS Nano* 14(5):5543–5552
2. Fu S, Zhu C, Song J et al (2016) PdCuPt nanocrystals with multi-branches for enzyme-free glucose detection. *ACS Appl Mater Interfaces* 8(34):22196–22200
3. Wang C, Nie XG, Shi Y et al (2017) Direct plasmon-accelerated electrochemical reaction on gold nanoparticles. *ACS Nano* 11(6):5897–5905
4. Rafai'deen T, Baranton S, Coutanceau C (2019) Highly efficient and selective electrooxidation of glucose and xylose in alkaline medium at carbon supported alloyed PdAu nanocatalysts. *Appl Catal B Environ* 243:641–656
5. Chen M, Cao X, Chang K et al (2021) A novel electrochemical non-enzymatic glucose sensor based on Au nanoparticle-modified indium tin oxide electrode and boronate affinity. *Electrochim Acta* 368:137603
6. Li Q, Shao Z, Han T et al (2019) A high-efficiency electrocatalyst for oxidizing glucose: ultrathin nanosheet co-based organic framework assemblies. *ACS Sustain Chem Eng* 7(9):8986–8992
7. Wang L, Yu H, Zhang Q et al (2021) NiCo–NiCoO₂/carbon hollow nanocages for non-enzyme glucose detection. *Electrochim Acta* 381:138259
8. Mao H, Cao Z, Guo X et al (2019) Ultrathin NiS/Ni(OH)₂ nanosheets filled within ammonium polyacrylate-functionalized polypyrrole nanotubes as an unique nanoconfined system for nonenzymatic glucose sensors. *ACS Appl Mater Interfaces* 11(10):10153–10162
9. Wang Y, Shao Y, Matson DW et al (2010) Nitrogen-doped graphene and its application in electrochemical biosensing. *ACS Nano* 4(4):1790–1798
10. Shu Y, Li B, Chen J et al (2018) Facile synthesis of ultrathin nickel-cobalt phosphate 2D nanosheets with enhanced electrocatalytic activity for glucose oxidation. *ACS Appl Mater Interfaces* 10(3):2360–2367
11. Peng X, Nie X, Zhang L et al (2020) Carbon-coated tungsten oxide nanospheres triggering flexible electron transfer for efficient electrocatalytic oxidation of water and glucose. *ACS Appl Mater Interfaces* 12(51):56943–56953
12. Liang T, Zou L, Guo X et al (2019) Rising mesopores to realize direct electrochemistry of glucose oxidase toward highly sensitive detection of glucose. *Adv Funct Mater* 29(44):1903026
13. Rui N, Zhang X, Zhang F et al (2021) Highly active Ni/CeO₂ catalyst for CO₂ methanation: preparation and characterization. *Appl Catal B Environ* 282:119581
14. Wang Z, Zhang Y, Neyts EC et al (2018) Catalyst preparation with plasmas: how does it work? *ACS Catal* 8(3):2093–2110
15. Kortshagen UR, Sankaran RM, Pereira RN et al (2016) Nonthermal plasma synthesis of nanocrystals: fundamental principles, materials, and applications. *Chem Rev* 116(18):11061–11127
16. Liu P, Niu L, Men YL et al (2023) Overturning photoreduction product of CO₂ by defect- and COOH-functionalized multi-wall carbon nanotubes. *Appl Catal B Environ* 320:121985
17. Men YL, Liu P, Liu Y et al (2022) Noble-metal-free WO₃-decorated carbon nanotubes with strong W–C bonds for boosting an electrocatalytic glucose oxidation reaction. *Ind Eng Chem Res* 61(12):4300–4309
18. Zhao B, Zhao Y, Liu P et al (2023) Boosting the adsorption and removal of dye from water by COOH-functionalized carbon nanotubes. *Green Chem Eng* 4(1):88–98
19. Ali S, Rehman SAU, Shah IA et al (2019) Efficient removal of zinc from water and wastewater effluents by hydroxylated and carboxylated carbon nanotube membranes: Behaviors and mechanisms of dynamic filtration. *J Hazard Mater* 365:64–73
20. Usman Farid M, Luan HY, Wang Y et al (2017) Increased adsorption of aqueous zinc species by Ar/O₂ plasma-treated carbon nanotubes immobilized in hollow-fiber ultrafiltration membrane. *Chem Eng J* 325:239–248
21. Hong S, Lee DM, Park M et al (2020) Controlled synthesis of N-type single-walled carbon nanotubes with 100% of quaternary nitrogen. *Carbon* 167:881–887
22. Basiuk EV, Huerta L, Basiuk VA (2019) Noncovalent bonding of 3d metal(II) phthalocyanines with single-walled carbon nanotubes: a combined DFT and XPS study. *Appl Surf Sci* 470:622–630
23. Bensaïder A, Lau Truong S, Seydou M et al (2017) Efficient covalent modification of multiwalled carbon nanotubes with diazotized dyes in water at room temperature. *Langmuir* 33(27):6677–6690
24. Garland BM, Fairley N, Strandwitz NC et al (2022) A study of in situ reduction of MoO₃ to MoO₂ by X-ray photoelectron spectroscopy. *Appl Surf Sci* 598:153827
25. Zhang F, Dong X, Cheng X et al (2019) Enhanced gas-sensing properties for trimethylamine at low temperature based on MoO₃/Bi₂Mo₃O₁₂ hollow microspheres. *ACS Appl Mater Interfaces* 11(12):11755–11762
26. Wang Z, Liu Y, Cheng Y et al (2022) Fast and efficient electrocatalytic oxidation of glucose triggered by Cu₂O–CuO nanoparticles supported on carbon nanotubes. *Front Chem* 10:998812

27. Beden B, Largeaud F, Kokoh KB et al (1996) Fourier transform infrared reflectance spectroscopic investigation of the electrocatalytic oxidation of D-glucose: identification of reactive intermediates and reaction products. *Electrochim Acta* 41(5):701–709
28. Holade Y, Servat K, Napporn TW et al (2016) Highly selective oxidation of carbohydrates in an efficient electrochemical energy converter: cogenerating organic electrosynthesis. *Chemsuschem* 9(3):252–263
29. Lei HW, Wu B, Cha CS et al (1995) Electro-oxidation of glucose on platinum in alkaline solution and selective oxidation in the presence of additives. *J Electroanal Chem* 382(1–2):103–110
30. Ganji MD, Bakhshandeh A (2013) Electronics and structural properties of single-walled carbon nanotubes interacting with a glucose molecule: ab initio Calculations. *Commun Theor Phys* 60(3):341–347



Yu-Long Men obtained his BS, MS, and Ph.D. from Hainan University, Tongji University and Shanghai Jiao Tong University. He has been a postdoctoral fellow in the department of Chemistry of SJTU since 2023. His research interests are focused on the design and synthesis of noble-metal-free catalyst applied in thermocatalytic and photocatalytic CO₂ capture and conversion, electrocatalytic glucose detection and conversion. He has authored 3 invention patents and published 25 SCI articles.



Lei Zhang obtained his BS from Wuhan University in 2011 and Ph.D. from the Second Military Medical University in 2016. He is an attending doctor of Changhai Hospital, the first affiliated hospital of Naval Medical University. His research interests focus on the incidence, development, treatment and prognosis of aortic dissection. He has been funded twice by National Natural Science Foundation of China, published 27 SCI articles, authorized 5 invention patents and 11 utility patents.



Peng Liu obtained his Ph.D. degree from Shanghai Jiao Tong University in 2023. Now, he has been a postdoctoral fellow in the department of Chemistry and Chemical Engineering of SJTU since 2023. His main research interests are focused on the design and synthesis of plasma-assisted preparation of nanomaterials. He has authored 6 invention patents and published 24 SCI articles.

Authors and Affiliations

Yu-Long Men¹ · Ning Dou² · Yiyi Zhao¹ · Yan Huang¹ · Lei Zhang³ · Peng Liu¹

✉ Yu-Long Men
menyulong1988@sjtu.edu.cn

✉ Lei Zhang
heatstones@yeah.net

✉ Peng Liu
liupeng715@sjtu.edu.cn

¹ Department of Chemical Engineering, School of Chemistry and Chemical Engineering, Shanghai Jiao Tong University, Shanghai 200240, China

² Department of Thyroid Breast and Vascular Surgery, Shanghai Fourth People's Hospital Affiliated to Tongji University School of Medicine, Shanghai 200081, China

³ Department of Vascular Surgery, Changhai Hospital, Naval Medical University, Shanghai 200433, China